Dalton Transactions

ROYAL SOCIETY OF CHEMISTRY

PAPER

View Article Online
View Journal | View Issue

Check for updates

Cite this: *Dalton Trans.*, 2021, **50**, 17573

Macrocycle based dinuclear dysprosium(III) single molecule magnets with local D_{5h} coordination geometry†

Jianfeng Wu,[a,b] Serhiy Demeshko,[a] Sebastian Dechert[a] and Franc Meyer *[a]

Received 23rd August 2021,
Accepted 8th November 2021

DOI: 10.1039/d1dt02815d

rsc.li/dalton

Targeted approaches for manipulating the coordination geometry of lanthanide ions are a promising way to synthesize high-performance single-molecule magnets (SMMs), but most of the successful examples reported to date focus on mononuclear complexes. Herein, we describe a strategy to assemble dinuclear SMMs with Dy^{III} ions in approximate D_{5h} coordination geometry based on pyrazolate-based macrocyclic ligands with two binding sites. A **Dy_4** complex with a rhomb-like arrangement of four Dy^{III} as well as two dinuclear complexes having axial chlorido ligands (**Dy_2·Cl** and **Dy_2^*·Cl**) were obtained; in the latter case, substituting Cl^- by SCN^- gave **Dy_2·SCN**. Magneto-structural studies revealed that the μ-OH bridges with short Dy–O bonds dominate the magnetic anisotropy of the Dy^{III} ions in centrosymmetric **Dy_4** to give a vortex type diamagnetic ground state. Dynamic magnetic studies of **Dy_4** identified two relaxation processes under zero field, one of which is suppressed after applying a dc field. For complexes **Dy_2·Cl** and **Dy_2^*·Cl**, the Dy^{III} ions feature almost perfect D_{5h} environment, but both complexes only behave as field-induced SMMs (U_{eff} = 19 and 25 K) due to the weak axial Cl^- donors. In **Dy_2·SCN** additional MeOH coordination leads to a distorted D_{2d} geometry of the Dy^{III} ions, yet SMMs properties at zero field are observed due to the relatively strong axial ligand field provided by SCN^- (U_{eff} = 43 K). Further elaboration of preorganizing macrocyclic ligands appears to be a promising strategy for imposing a desired coordination geometry with parallel orientation of the anisotropy axes of proximate Dy^{III} ions in a targeted approach.

Introduction

Lanthanides have attracted increasing attention in the field of single-molecule magnetism during the past two decades,[1] mostly due to their large magnetic moments and their often highly anisotropic character, which favors large energy barriers and high blocking temperatures for the magnetization relaxation.[2] According to crystal field theory and electrostatic models,[3] Dy^{III} ions in an axial ligand field with D_{4d},[4] D_{5h},[5] D_{6h},[6] and $C_{\infty v}$[7] symmetry are likely to feature particularly large energy barriers and a low probability for quantum tunnelling of the magnetization (QTM). In light of these conceptual considerations, numerous dysprosium-based single-molecule magnets (SMMs) with excellent magnetic properties and hysteretic behaviour have been synthesized, reaching blocking temperatures up to 80 K.[8] However, these high-performance Dy-based SMMs are mostly limited to mononuclear systems.

An increasingly pursued strategy for enhancing the SMM properties aims at promoting magnetic interactions in complexes with several proximate Dy^{III} ions.[9] Due to the usually high coordination numbers and flexibility of the coordination spheres of lanthanide ions,[10] however, it is quite challenging to simultaneously control the geometry and ligand field in such oligonuclear complexes. Dinuclear systems represent the simplest case of oliogo- and polymetallic 4f element SMMs, and manipulating their ligand field and magnetic interactions appears to be comparatively facile.[11] In many reported dinuclear Dy^{III} complexes the two Dy^{III} ions are ferromagnetically coupled,[12] which reduces the QTM probability. In most of these complexes, however, the Dy^{III} ions are surrounded by more than two ligands and reside in rather distorted coordination geometries of low symmetry, often approximating D_{2d}[13] and C_{2v},[14] which is unfavourable for establishing an axial ligand field of the Dy^{III} ions and usually does not result in a large anisotropy or high blocking temperature.

---

[a] *Institut für Anorganische Chemie, Universität Göttingen, Tammannstr. 4, D-37077 Göttingen, Germany. E-mail: franc.meyer@chemie.uni-goettingen.de*

[b] *School of Chemistry and Chemical Engineering, Northwestern Polytechnical University, Xi'an 710072, P. R. China*

† Electronic supplementary information (ESI) available: IR spectra, XRD, and TGA are depicted in Fig. S1–S5. Crystallographic data are listed in Table S1 and Fig. S6–S9. Selected bond lengths and angles are listed in Tables S2–S5. SHAPE calculations are given in Tables S6–S8 and Fig. S10–S12. The *M vs. H* plots are presented in Fig. S13–S16. Ac susceptibilities are presented in Fig. S17–S23. Magellan calculations are given in Tables S16 and Fig. S24–S26. CCDC 2103370–2103373. For ESI and crystallographic data in CIF or other electronic format see DOI: 10.1039/d1dt02815d

To realize axial ligand fields in dinuclear complexes in a targeted approach, careful ligand design is essential. On the one hand, the ligand should allow for high coordination numbers and should not be in conflict with the flexible nature of the 4f metal ions' coordination spheres. On the other hand, the coordinating atoms of the ligand scaffold should be precisely arranged to enforce a specific coordination symmetry. To meet the two demands simultaneously, one efficient way is to place two strong donor ligands at the axial directions to establish the dominating anisotropy axis while surrounding the metal ion with weak field ligands in the equatorial plane to provide the high coordination number that is favored by Dy^{III} ions. To that end, planar macrocycle-based scaffolds with weak N or O donors within the equatorial plane, which direct the binding of stronger exogenous donor ligands to the axial positions, show great promise for Dy^{III} SMMs with large anisotropy. In this context, a few mononuclear dysprosium SMMs based on crownether[15] or metallacrown ligands have been reported.[16] Recently, Tong *et al.* achieved an approximately collinear arrangement of the Dy^{III}–Dy^{III} Ising moments of two Dy^{III} monomers that are based on Cu_5 metallacrowns with local D_{5h} geometry; their magnetic signatures are a result of both antiferromagnetic coupling within the Cu_5 metallacrowns as well as ferromagnetic Dy⋯Cu and Dy⋯Dy interactions.[17] In order to exclude magnetic contributions from an open-shell metallacrown, the construction of dinuclear Dy^{III} SMMs from planar macrocyclic ligands providing two pentadentate binding sites, combined with variation of axial coligands, appears to be a promising strategy to establish a proper ligand field of the Dy^{III} ions in D_{5h} coordination geometry.

With these thoughts in mind, and in view of our group's long history in the development of dinucleating pyrazolate ligands,[18,19] we set out to synthesize dinuclear Dy^{III} SMMs using bis(pyrazolato)-bridged macrocycles with two $\{N_5\}$ donor compartments that provide the metal ions' equatorial coordination sphere. To that end, we conducted metal ion templated [2 + 2] ring formation reactions between pyrazole 3,5-dialdehyde and linear triamines. Unexpectedly, however, macrocycle formation did not occur and a Dy_4 complex was obtained from these reactions (Scheme 1). We then turned to the corresponding pyrazole 3,5-diketone building block, which indeed led to the anticipated macrocycle-based dinuclear Dy^{III} complexes (Scheme 2). All new complexes have been comprehensively characterized structurally and magnetically, and magneto-structural considerations have been used to rationalize the findings. The results are presented and further prospects of the approach are discussed in this paper.

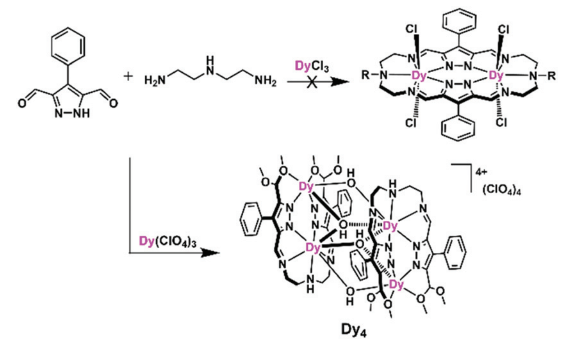

Scheme 1 Schematic drawing of the assembly of Dy_4.

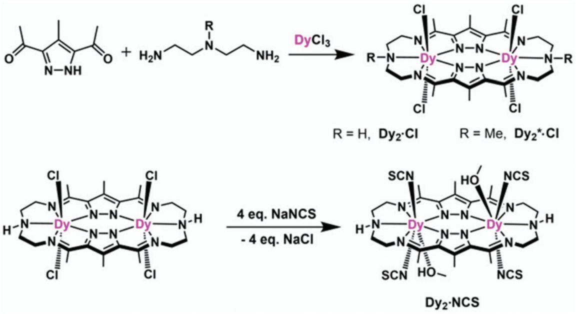

Scheme 2 Schematic drawing of the assemblies of $\mathbf{Dy_2{\cdot}Cl}$, $\mathbf{Dy_2^{*}{\cdot}Cl}$, and $\mathbf{Dy_2{\cdot}SCN}$.

Results and discussion

Synthesis and structural characterization of $\mathbf{Dy_4}$

Our initial objective was to assemble dinuclear Dy^{III} complexes with macrocyclic ligands that are derived from the condensation of pyrazole 3,5-dialdehydes with diethylentriamine *via* a templated [2 + 2] ring formation reaction (Scheme 1). When using 4-phenyl-3,5-dicarbaldehyde-1*H*-pyrazole, however, the unexpected product $[Dy_4(\mu_3\text{-}OH)_2L^1{}_2(\mu_2\text{-}OH)_2(DMF)_4]\cdot 4ClO_4$ (**Dy_4**; H_2L^1 = bis((5-dimethoxymethyl-4-phenyl-1*H*-pyrazolmethylene-amino)ethyl)-amine) was isolated. Herein, the ligand H_2L^1 was formed from the [1 + 2] condensation of one diethylenetriamine with two pyrazole dialdehyde building blocks and acetal formation with methanol at the remaining aldehyde functions (Scheme S1†). Such acetal formation is common for aldimine condensation reactions when alcohols are present.[20] The pyrazole-based ligand is deprotonated during the complexation with Dy^{III} ions.

Complex **Dy_4** was isolated as yellow crystals by slow diffusion of diethyl ether into a DMF solution of the crude product. Single-crystal X-ray diffraction revealed that complex **Dy_4** crystallizes in the monoclinic space group $P2_1/n$ (Table S1†) and shows centrosymmetry with the asymmetric unit containing half of the complex: one ligand, two Dy^{III} ions, two coordinated DMF, two μ-OH bridges, and two ClO_4^-. The presence of OH groups is corroborated by a band at 3582 cm^{-1} for the O–H stretch in the IR spectrum of solid **Dy_4** (Fig. S1†). Each $[L^1]^{2-}$ ligand strand in **Dy_4** is bent to bind two Dy^{III} ions, one in the inner $\{N_5\}$ and one in the outer $\{N_2O_2\}$ pocket, forming a Dy_2 synthon with two additional DMF molecules coordinated to the Dy^{III} ions. Two Dy_2 subunits are connected by two μ_3-OH and two μ-OH groups, forming **Dy_4** with the four Dy^{III} ions arranged in a rhomb-like topology (Fig. 1). Four

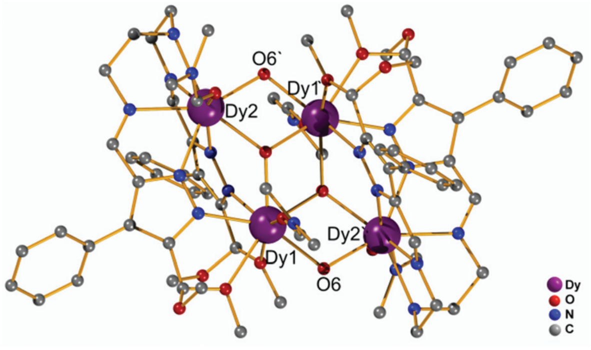

Fig. 1 Molecular structure of the cation of $\mathbf{Dy_4}$. Hydrogen atoms and counteranions have been omitted for clarity.

ClO_4^- are present in the lattice to balance the positive charges (Fig. S6†). Due to the centrosymmetric nature of the molecule, the four Dy^{III} ions are in one plane. The two μ_3-OH are located above and below this plane of the Dy_4 rhomb, and the μ-OH each connect two Dy^{III} ions at the edges of the rhomb. Selected atom distances and angles are listed in Tables S2 and S3.† Comparing the bond lengths, we find that the Dy–O6 (μ-OH) bonds (2.26 and 2.27 Å) are much shorter than the other coordination bonds. The anisotropy axes of Dy^{III} ions are usually close to the shortest coordination bonds, which provides an efficient single/double atomic axial crystal field.[21] Therefore, in our case, the magnetic anisotropies of the Dy^{III} ions are probably related to the μ-OH bridges.

Apart from the bond lengths, the individual coordination geometry also influences the anisotropy of Dy^{III} ions. In complex $\mathbf{Dy_4}$, both Dy1 and Dy2 are eight coordinate but in different coordination environments (Fig. S10†). We used SHAPE[22] to analyze the coordination geometry of the Dy^{III} ions. As shown in Table S6,† the geometry of Dy1 is best described as a distorted square antiprism (D_{4d}) with a CShM value of 1.36, while the coordination geometry for Dy2 is close to a biaugmented trigonal prism (C_{2v}) with a CShM value of 1.90. Another factor that influences the magnetic properties of the complex is the magnetic coupling between Dy^{III} ions.[23] In $\mathbf{Dy_4}$ the Dy⋯Dy distances are in the range of 3.72–3.81 Å, which is expected to give rise to weak intramolecular magnetic interactions.

Synthesis and structural characterization of $\mathbf{Dy_2{\cdot}Cl}$ and $\mathbf{Dy_2^*{\cdot}Cl}$

Complexes $[Dy_2L^2Cl_4]$ ($\mathbf{Dy_2{\cdot}Cl}$; H_2L^2 = hexamethyl-hexaaza-dipyrazolacycloicosaphane-2,9,12,19-tetraene) and $[Dy_2L^3Cl_4]$ ($\mathbf{Dy_2^*{\cdot}Cl}$; H_2L^3 = (octamethyl-hexaaza-dipyrazolacycloicosaphane-2,9,12,19-tetraene) were obtained from the *in situ* reaction of 3,5-diacetyl-4-methyl-1*H*-pyrazole with diethylenetriamine (for $\mathbf{Dy_2{\cdot}Cl}$) or *N*,*N*-bis(2-aminoethyl)methylamine (for $\mathbf{Dy_2^*{\cdot}Cl}$) and $DyCl_3{\cdot}6H_2O$ (Scheme 2). Herein, the reaction of the diketone with a diamine in methanol forms the macrocyclic ligands rather than an open chain ligand bearing acetal groups as was observed for $\mathbf{Dy_4}$, which we attribute to the different propensity of ketones *vs.* aldehydes to react with alcohols. X-ray diffraction (XRD) quality crystalline material of both complexes was obtained upon recrystallization from methanol. The purity of the bulk samples was confirmed by powder XRD analyses (Fig. S3 and S4†). Thermogravimetric analyses evidenced that the compounds are stable up to 350 °C (Fig. S5†), which is beneficial for potential applications. $\mathbf{Dy_2{\cdot}Cl}$ and $\mathbf{Dy_2^*{\cdot}Cl}$ both crystallize in the monoclinic space group $P2_1/c$ with similar cell parameters (Table S1†). As shown in Fig. 2a and b, structural features of the two complexes are also very similar. Their molecular entities are centrosymmetry, containing one macrocyclic ligand, two Dy^{III} ions, and four coordinated Cl^-. The central pyrazolate bridges of the ligand are coplanar and span two $\{N_5\}$ pockets that each hosts a Dy^{III} ion, as was anticipated. The Cl^- anions coordinate to Dy^{III} in axial positions above and below the ligand plane, forming an overall pentagonal bipyramidal (D_{5h}) coordination polyhedron (Fig. 2). In the crystal packing, the Cl^- ligands are in contact with the nearest methyl groups from neighboring molecules, presumably *via* weak hydrogen bonds (C–H⋯Cl distances in the range of 2.50–2.87 Å) to constitute 2D ($\mathbf{Dy_2{\cdot}Cl}$, Fig. S7†) and 3D frameworks ($\mathbf{Dy_2^*{\cdot}Cl}$, Fig. S8†) in the lattice. The Dy–N bond lengths in the molecular structures are in the range of 2.44–2.48 Å and 2.45–2.55 Å for $\mathbf{Dy_2{\cdot}Cl}$ and $\mathbf{Dy_2^*{\cdot}Cl}$ (Tables S4 and S5†), respectively. The Dy–Cl bond lengths in the two complexes are close to 2.61 Å, which is much longer than the Dy–N distances, indicating axially elongated pentagonal bipyramidal coordination spheres. The Cl–Dy–Cl angles are 169.18 and 174.17° for $\mathbf{Dy_2{\cdot}Cl}$ and $\mathbf{Dy_2^*{\cdot}Cl}$, respectively. The almost linear Cl–Dy–Cl arrangement reflects the rather small distortion of the D_{5h} coordination geometry.

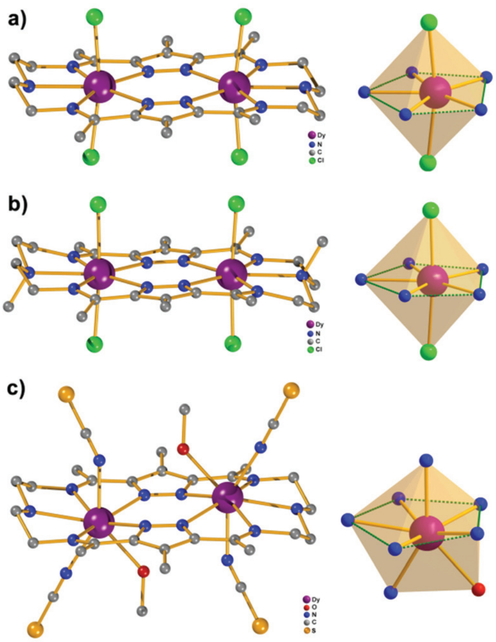

Fig. 2 Structure views of complexes $\mathbf{Dy_2{\cdot}Cl}$ (a), $\mathbf{Dy_2^*{\cdot}Cl}$ (b), and $\mathbf{Dy_2{\cdot}NCS}$ (c). The orange spheres represent the coordination polyhedron of the relevant Dy^{III} ion in the complexes. Hydrogen atoms are omitted for clarity.

To quantify the distortion of the coordination geometry, SHAPE analyses were carried out for the two complexes. The results are listed in Table S7.† As expected, the coordination polyhedra of the Dy^{III} ions are close to a pentagonal bipyramid (D_{5h}) with CShM values of 0.80 and 0.69 for **Dy_2·Cl** and **Dy_2^*·Cl**, respectively. The small deviations indicate a successful control of the coordination geometry by these bis(pyrazolato) based macrocycle ligands, in accordance with the strategy outlined in the Introduction. Particularly, this is the first example of hosting two D_{5h} coordinated Dy^{III} ions within one macrocyclic ligand at rather short Dy⋯Dy distances (4.73 and 4.77 Å for **Dy_2·Cl** and **Dy_2^*·Cl**, respectively). However, the weak Cl^- donors at the axial positions result in a stretched D_{5h} coordination environment, which is unfavorable for the anisotropy of the oblate Dy^{III} ion. To modulate the ligand field and optimize potential SMMs properties (see below), substitution of the Cl^- anions with stronger anionic N-donors was pursued in the case of complex **Dy_2·Cl**.

Synthesis and structural characterization of Dy_2·NCS

Complex $[Dy_2L^2NCS_4(MeOH)_2]$ (**Dy_2·NCS**) was obtained from **Dy_2·Cl** by ligand substitution upon addition of NH_4SCN, replacing Cl^- by NCS^- (Scheme 2). X-ray diffraction on single crystals obtained from methanol revealed that **Dy_2·NCS** crystallizes in the triclinic space group $P\bar{1}$ (Table S1†); the molecular structure is shown in Fig. 2c. It features one dianionic macrocyclic ligand $[L^2]^{2-}$, two Dy^{III} ions residing in the $\{N_5\}$ pockets, four SCN^-, and two coordinated methanol solvent molecules (Fig. 2 and S9†). The $\{L^2Dy_2\}$ core found in **Dy_2·Cl** is preserved in **Dy_2·NCS**, but two SCN^- are now N-bound above and below the roughly planar core with Dy–N bond lengths of 2.40 and 2.42 Å. These axial bonds are shorter than the equatorial Dy–N bonds involving the macrocyclic ligand $[L^2]^{2-}$ (2.45–2.55 Å). The two additional methanol ligands give rise to eight coordinate Dy^{III} ions and move the Dy^{III} 0.4 Å out of the equatorial $\{N_5\}$ plane towards the side of the methanol. Hence the N^{SCN}–Dy–N^{SCN} angles of 149.5° reflect strong deviation from a linear arrangement (Table S4†). SHAPE analysis suggests that the Dy^{III} ions exhibit a distorted triangular dodecahedron geometry (D_{2d}) with a CShM value of 2.6. In comparison with **Dy_2·Cl** and **Dy_2^*·Cl**, the Dy^{III} ions in **Dy_2·NCS** reside in a lower symmetry coordination environment, yet the SCN^- at the axial positions give rise to short Dy–N distances and a relatively strong ligand field; the latter was expected to prove beneficial in terms of SMM properties.

Static magnetic properties

To explore the magnetic properties of **Dy_4**, direct current (dc) magnetic susceptibility measurements were carried out on polycrystalline samples under an applied field of 1000 Oe in the temperature range 2–210 K. As shown in Fig. 3, the $\chi_M T$ product (χ_M is molar magnetic susceptibility) at 210 K is 52.97 cm^3 K mol^{-1}, which is slightly smaller than the expected value for four Dy^{III} ions in the free-ion approximation (56.68 cm^3 K mol^{-1}, $^6H_{15/2}$, $g = 4/3$ for Dy^{III} ion). Upon cooling, the $\chi_M T$ product decreases gradually before dropping more quickly below 15 K, and it reaches 22.18 cm^3 K mol^{-1} at 2 K. The drop of $\chi_M T$ at low temperatures can be attributed to the depopulation of the excited m_J sublevels of the ground J states of the Dy^{III} ions, the onset of magnetic blocking, and a dominating diamagnetic ground state, which might result from antiferromagnetic interactions or from the toroidal arrangement of the magnetic axes of the individual Dy^{III} ions.[24] Under a 5000 Oe dc field, the temperature-dependent $\chi_M T$ data shows a similar profile. A plot of the molar magnetization (M) *vs.* H for **Dy_4** at 2 K (Fig. S13†) shows a relatively slow increase near zero field and a fast increase when rising the temperature (Fig. S13†), which is indicative of STM behavior. This is followed by a linear increase of M at high fields, reaching the value of 19.38 μ_B at 5 T, which is close to the expected value of 20 μ_B for four Dy^{III} ions in a pure $m_J = |\pm 15/2>$ ground state.

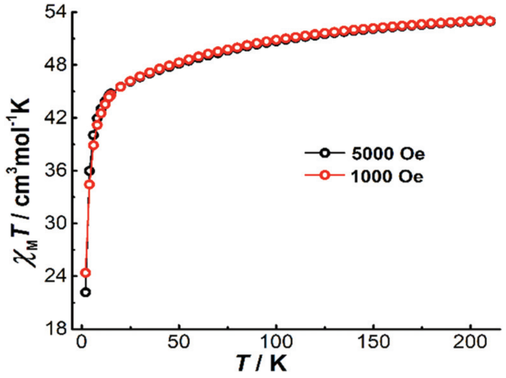

Fig. 3 Temperature dependence of the product $\chi_M T$ for **Dy_4** at indicated fields between 2 and 210 K.

To gain more insight into the magnetic properties of **Dy_4**, the anisotropy axes of the Dy^{III} ions were calculated by the Magellan program[25] based on the structure determined crystallographically. As shown in Fig. 4, the magnetic anisotropy axes of all Dy^{III} ions are close to Dy–O6 directions. This is mainly because of the short Dy–O bonds giving a relatively stronger

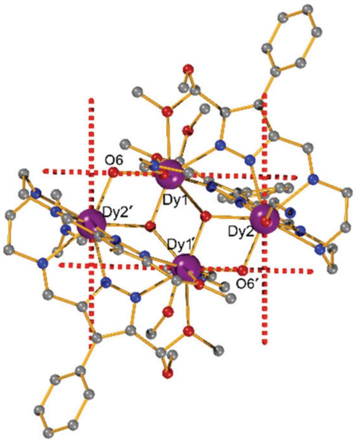

Fig. 4 Orientations of the main magnetic axes of the local magnetizations in the ground state of **Dy_4**.

ligand field that dominates the orientation of the local magnetic moments. Overall, the anisotropy axes of the four Dy^{III} ions are arranged in a toroidal fashion, suggesting the potential existence of single-molecule toroic (SMT) behavior.[24b,26] However, this calculation is based on an electrostatic model that does not include any intramolecular interaction and excited states, therefore future quantitative evaluation of the ground states and of the magnetic interaction J through *ab initio* calculations is desirable.[26a,27]

For the dinuclear complexes **Dy$_2$·Cl**, **Dy$_2$*·Cl**, and **Dy$_2$·NCS**, the variable temperature $\chi_M T$ data show values of 27.63, 27.67, and 27.30 cm^3 K mol^{-1}, respectively, at 210 K (Fig. 5). These values are close to the expected one for two Dy^{III} ions in the free-ion approximation (28.34 cm^3 K mol^{-1}). Upon cooling, $\chi_M T$ decreases gradually before dropping more quickly below 50 K to reach 13.70 (**Dy$_2$·Cl**), 14.09 (**Dy$_2$*·Cl**), and 13.45 cm^3 K mol^{-1} (**Dy$_2$·NCS**) at 2 K. The drop of the $\chi_M T$ product at low temperatures can be ascribed to dominating antiferromagnetic interactions between the two Dy^{III} ions. Plots of the molar magnetization (M) *vs.* H at 2 K (Fig. S14 and S15†) show a sharp increase at low fields followed by a linear increase at high fields, reaching the values of 10.24 (**Dy$_2$·Cl**), 10.57 (**Dy$_2$*·Cl**), and 11.51 μ_B (**Dy$_2$·NCS**) at 5 T; these values are close to the expected value 10 μ_B for two Dy^{III} ions in a pure $m_J = |\pm 15/2>$ ground state.

Dynamic magnetic properties

Alternating current (ac) susceptibility measurements were performed on **Dy$_4$** under an oscillating field of 3.0 Oe to study the dynamic magnetic properties. Two overlapped out-of-phase (χ'') peaks at 9 and 14 K are detected in the temperature-dependent ac susceptibility at zero dc field (Fig. S17†), suggesting the presence of two relaxation processes. This behavior usually occurs in polynuclear SMMs that contain more than one asymmetric Dy^{III} ion.[28] In **Dy$_4$**, the Dy^{III} ions are in two different coordination environments, *viz.* a distorted square antiprism (D_{4d}) and a biaugmented trigonal prism (C_{2v}) as described above, which might translate into two relaxation processes. To further explore these relaxation processes, field-dependent ac measurements were carried out at 9 and 14 K (Fig. S18†). A maximum of the χ'' signal is observed around 800 Oe for the measurement at 9 K, while a minimum is detected at the same field for the measurement at 14 K, suggesting that the application of a dc field can efficiently regulate the relaxation process. As shown in Fig. S18,† only one temperature-dependent χ'' peak at 9 K is observed under 800 Oe field. Compared with the measurement without field, the χ'' signal at 14 K is suppressed. Temperature- and frequency-dependent χ'' signals show broad peaks under zero dc field (Fig. 6 and Fig. S19†). After applying an 800 Oe dc field, the broad χ'' peaks become sharper, indicating only one relaxation process involved in the magnetic moment reversal.

The Cole–Cole plots represented as χ'' *versus* χ' at zero applied field (Fig. 7, top) show broad semi-circular profiles, suggesting multiple relaxation processes. After applying an 800 Oe dc field, however, the Cole–Cole plots evolve into single

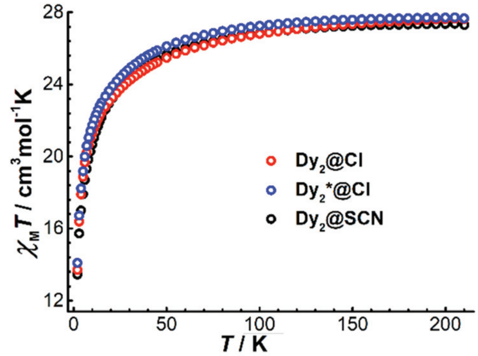

Fig. 5 Temperature dependence of the product $\chi_M T$ for **Dy$_2$·Cl**, **Dy$_2$*·Cl**, and **Dy$_2$·NCS** at 5000 Oe between 2 and 210 K.

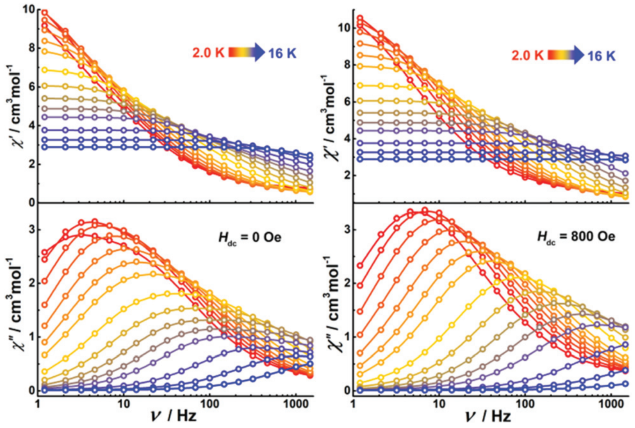

Fig. 6 Frequency-dependent ac susceptibility of **Dy$_4$** under zero (left) and 800 Oe (right) dc field.

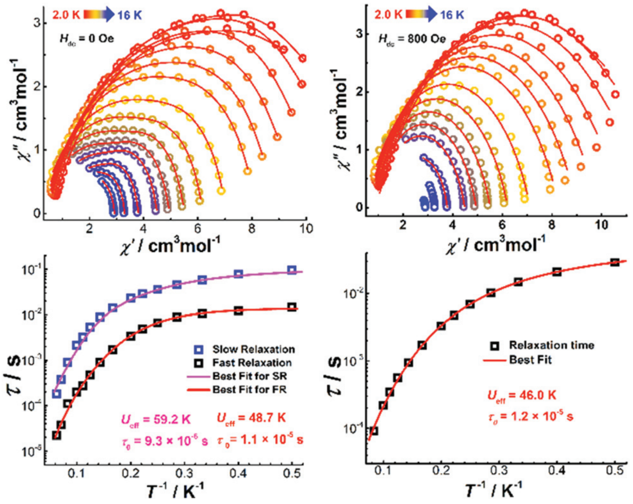

Fig. 7 The Cole–Cole diagrams (top) and τ *vs.* T^{-1} plots (bottom) under zero (left) and 800 Oe (right) dc field for **Dy$_4$**. The solid lines indicate the best fits.

semi-circular curves, indicative of a single relaxation process. Fitting the Cole–Cole plots at zero-field with the CC-FIT program[29] by assuming a double relaxation Debye model confirms the presence of two relaxation processes. Fitting of the data obtained under an 800 Oe field gives one relaxation process. The relevant fitting parameters are listed in Tables S9 and S10.†

The relaxation time (τ) for magnetic moment reversal was extracted from the best fits of the Cole–Cole plots. We fitted the relevant τ *versus* $1/T$ plots with the following equation:[30]

$$\frac{1}{\tau_{\mathrm{obs}}} = \frac{1}{\tau_{\mathrm{QTM}}} + AH^4T + CT^n + \tau_0^{-1}\exp(-U_{\mathrm{eff}}/T) \qquad (1)$$

where $1/\tau_{\mathrm{QTM}}$, AH^4T, CT^n and $\tau_0^{-1}\exp(-U_{\mathrm{eff}}/T)$ represent quantum tunneling, direct, Raman and Orbach relaxation processes,[31] respectively. The best fit gave the anisotropy barriers $U_{\mathrm{eff}} = 59.2$ K with $\tau_0 = 9.3 \times 10^{-6}$ s for the slow relaxation phase (SR) and $U_{\mathrm{eff}} = 48.7$ K and $\tau_0 = 1.1 \times 10^{-5}$ s for the fast relaxation phase (FR). Other parameters obtained from the fitting are listed in Table S11.† For the relaxation under 800 Oe dc field, a similar fitting using the above equation was carried out and gave the anisotropy barrier $U_{\mathrm{eff}} = 46$ K and $\tau_0 = 1.2 \times 10^{-5}$ s (Fig. 7). The energy barrier, especially the relaxation times in the low-temperature region, is found to be comparable with the relevant values of the FR phase under zero dc field (Tables S10 and S11†). Generally, the application of a dc field can suppress the quantum tunneling of the magnetization (QTM).[32] In the case of **Dy_4**, however, the dc field seems to suppress one of the thermal relaxation processes. We hypothesize that the two relaxation processes are from isolated and coupled relaxation pathways.[33] The coupled relaxation process is probably related to the intramolecular interactions, which could be suppressed by a proper dc field. Further investigation of the magnetic interactions and coupled magnetic states will require *ab initio* calculations.[23a,34]

Alternating current (ac) susceptibility measurements were also performed on the dinuclear complexes. Both **Dy_2·Cl** and **Dy_2^*·Cl** show an out of phase ac susceptibility signal (χ'') without peak under zero dc field (S20†), indicative of slow relaxation. We then performed field-dependent ac measurements at 2 K with a frequency of 1488 Hz to determine the optimal dc field. As shown in Fig. S21,† the ac plots are similar for the two complexes, the χ'' signal showing broad peaks around 300 and 1800 Oe as well as a trough at 1200 Oe. However, when ac measurements of the two complexes were performed at 300 Oe (Fig. S22†), the χ'' signal did not show any frequency-dependent peaks, and the relaxation time could not be extracted from the data. We suspect that the peaks at 300 and 1800 Oe originate from fast quantum tunneling of the magnetization (QTM), which is related to the cross of the energy gap. To suppress this relaxation process, a 1200 Oe dc field was then chosen and applied in all following ac susceptibility measurements. Indeed, the χ'' signal showed temperature- and frequency-dependent out of phase peaks under 1200 Oe dc field (Fig. 8), indicative of field-induced single molecule magnetic behavior. The profiles of the ac plots of the two complexes are similar because of the essentially identical structural features and coordination geometries. In contrast, complex **Dy_2·NCS** shows temperature and frequency-dependent χ'' peaks under zero dc field. Extracting the relaxation time (τ) for magnetic moment reversals from the Cole–Cole plots by using the CC-FIT software (Tables S12–S14†) and fitting the relevant τ *versus* $1/T$ plots yields the anisotropy barriers U_{eff} of 19.1, 25.1, and 43.1 K for **Dy_2·Cl**, **Dy_2^*·Cl**, and **Dy_2·NCS** (Fig. S23†), respectively. Other parameters obtained from the fitting are listed in Table S15.†

In **Dy_2·Cl** and **Dy_2^*·Cl**, the Dy^{III} ions are in almost perfect D_{5h} geometry. However, the energy barriers are not particularly high, and only field-induced SMM properties are observed. This can be ascribed to the weak Cl^- donors that lead to an axially elongated ligand field, which is unfavorable for the anisotropy of oblate Dy^{III} ions. When replacing the Cl^- with N-bound SCN^-, the resulting complex **Dy_2·SCN** shows SMMs properties even under zero field, as the SCN^- donors give relatively short Dy–N bonds and provide a relatively stronger axial ligand field. Although the coordination geometry of the Dy^{III} ions in **Dy_2·SCN** deviates from D_{5h}, the axial ligand field still plays an important role for dominating the anisotropy.

To further analyze the anisotropy of the dinuclear complexes, the anisotropy axes of the Dy^{III} ions were calculated using the Magellan program.[25] Assignments of the ligand charges are shown in Fig. S24.† The magnetic anisotropy axes of the Dy^{III} ions in complexes **Dy_2·Cl** and **Dy_2^*·Cl** are close to the Cl–Dy–Cl vectors (Fig. 9, Fig. S24†). In both complexes the

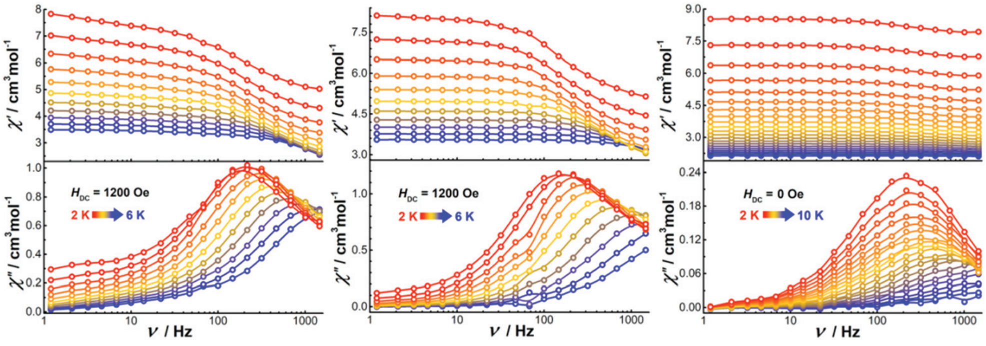

Fig. 8 Frequency-dependent ac susceptibility of **Dy_2·Cl** (left), **Dy_2^*·Cl** (middle), and **Dy_2·NCS** (right) under indicated fields and temperatures.

Dy–N distances are in the range of 2.44–2.55 Å and the Dy–Cl distances are 2.61 Å, as described above. The long axial coordination bonds result in a weak ligand field, in which large anisotropy could not be generated. However, the anisotropy of the Dy^{III} ions is still along the axial directions. In complex **Dy_2·NCS**, the anisotropy axes of the Dy^{III} ions are close to the Dy–N^{SCN} directions, specifically those involving the linearly bound SCN^- ligands, because of the relatively short Dy–N^{SCN} bonds (compared with the Dy–N bonds involving the equatorial ligand) that give rise to a roughly axial ligand field (Fig. 9).

Calculation of the anisotropy axes with the Magellan program uses an electrostatic model based on the crystallographically determined structures, where the magnetic anisotropy axes of the Dy^{III} ions are related to the negatively charged donors. To investigate the influence of the charges on the orientations of the anisotropy axes, we reduced the charge on Cl and N (in SCN^-) to half (Fig. S25†). As shown in Fig. S26,† the resulting anisotropy axes are still close to the directions mentioned above (with deviation angles of 1.0, 0.9, and 4.5° for **Dy_2·Cl**, **Dy_2^*·Cl**, and **Dy_2·NCS**, respectively, Table S16†). Overall, the anisotropy axes are directed roughly along the pseudo-C_5 axis defined by the equatorial plane that is constituted by the $\{N_5\}$ pockets of the macrocyclic ligand, and by the axial (pseudo) halide ligands; as a result, the anisotropy of the Dy^{III} ions appears to be dominated by the approximate local D_{5h} geometry, which is predetermined by the planar dinucleating macrocyclic scaffold.

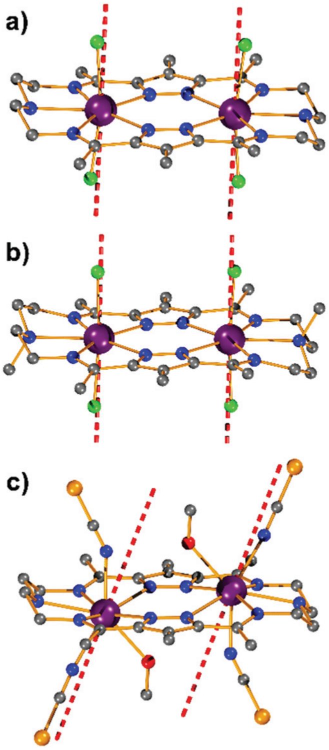

Fig. 9 Orientations of the main magnetic axes and local magnetizations of the ground state of the dinuclear complexes **Dy_2·Cl** (a), **Dy_2^*·Cl** (b), and **Dy_2·NCS** (c).

Conclusions

In summary, the template condensation of pyrazole-3,5-dicarbonyl synthons with linear triamines in the presence of dysprosium salts gave the expected bis(pyrazolato) bridged dinuclear Dy^{III} complexes **Dy_2·Cl** and **Dy_2^*·Cl** when using 3,5-diacetyl-4-methyl-1*H*-pyrazole and $DyCl_3·6H_2O$; the products feature a macrocyclic ligand providing two $\{N_5\}$ binding pockets and axial chlorides. However, the combination of 4-phenyl-3,5-dicarbaldehyde-1*H*-pyrazole and $Dy(ClO_4)_3·6H_2O$ resulted in a tetranuclear complex **Dy_4** with an open-chain ligand strand due to incomplete imine condensation and the presence of peripheral acetal groups. Studies of the magnetic properties and their analysis in view of the molecular structures suggested a toroidal orientation of the anisotropy axes and a diamagnetic ground state for **Dy_4** because of its centrosymmetric structure and the strongly coordinating μ-OH bridges in the plane of the rhomb-like Dy_4 arrangement. The dynamic magnetic properties of complex **Dy_4** revealed two relaxation processes under zero field, one of which can be suppressed after applying a weak dc field. The Dy^{III} ions in dinuclear complexes **Dy_2·Cl** and **Dy_2^*·Cl** exhibit almost perfect D_{5h} coordination geometry. Due to the weak Cl^- donors on the axial directions, however, both complexes only behave as field-induced SMMs. Replacement of the axial Cl^- donors by stronger SCN^- donors produced **Dy_2·SCN** that shows SMM signatures even at zero dc field, though additional MeOH ligands increase the Dy^{III} coordination number to 8 and decrease the local symmetry. Magnetostructural studies indicate that although the Dy^{III} ions are exposed to a weak ligand field, their more or less pronounced local D_{5h} geometry in the dinuclear complexes still dominates the orientation of the anisotropy axes.

Achieving high magnetic anisotropies that translate into favorable performances of SMMs is a consistent pursuit for chemists working in the field of molecular magnetism. A recent focus in Dy^{III} chemistry has been on the synthesis of mononuclear complexes with pronounced axial ligand field. Herein, a complementary strategy for enhancing the SMM properties has been pursued that targets preorganized dinuclear complexes in which a local D_{5h} geometry of the two Dy^{III} ions and a parallel orientation of their anisotropy axes are enforced by planar macrocyclic scaffolds with two pentadentate binding compartments. Although the SMM properties found for the present first examples of such Dy^{III}_2 complexes are not yet particularly impressive, the beneficial use of bis(pentadentate) macrocyclic scaffolds for controlling the Dy^{III} coordination chemistry has been demonstrated, and further modifications of the axial donors for modulating the ligand field appear to be promising. Work in the latter direction is underway in our laboratory.

Experimental

General synthetic considerations

All chemicals and solvents were commercially obtained and used as received without any further purification. 4-Phenyl-3,5-

dicarbaldehyde-1*H*-pyrazole and 3,5-diacetyl-4-methyl-1-*H*-pyrazole were synthesized under ambient conditions following a previously reported method.[35] IR measurements of solid samples were performed with a Cary 630 FTIR spectrometer equipped with Dial Path and Diamond ATR accessory and analyzed by FTIR MicroLab software. IR bands (Fig. S1 and S2†) were labeled according to their relative intensities with *vs*. (very strong), s (strong), m (medium), and w (weak). Powder X-ray diffraction measurements were recorded on Bruker D8 advance X-Ray diffractometer using Cu-Kα radiation. Thermogravimetric analyses were performed on a Netzsch STA449F3 TG-DSC instrument in the range of 25–1000 °C with a heating rate of 10 K min^{-1} under N_2 atmosphere. Elemental analyses were carried out using an Elementar Vario EL III instrument by the analytical laboratory of the Institute of Inorganic Chemistry at the Georg-August-University Göttingen.

Synthesis of Dy$_4$

The ligand and complex were synthesized *via* a one-pot procedure: a mixture of $Dy(ClO_4)_3·6H_2O$ (1 mmol) and 4-phenyl-3,5-dicarbaldehyde-1*H*-pyrazole (1 mmol) in 50 mL methanol was stirred and heated at 70 °C, then a solution of diethylenetriamine (1 mmol) in 20 mL methanol was added dropwise. After heating overnight at 70 °C, the solution was allowed to cool to room temperature. A yellow precipitate formed, which was separated by filtration, washed with methanol and dried under vacuum. Yellow crystals of complex **Dy$_4$** suitable for X-ray diffraction were obtained by slow diffusion of diethyl ether into a DMF solution of the crude product. Yield: 90 mg, (20%, based on metal salt). Elemental analysis (%) calcd for $[Dy_4(\mu_3\text{-}OH)_2L^1{}_2(\mu_2\text{-}OH)_2(DMF)_4]·4ClO_4$ ($C_{72}H_{102}Cl_4Dy_4N_{18}O_{32}$, MW = 2523.51): C, 34.27, H, 4.07, N, 9.99; found C, 33.57, H, 4.11, N, 9.71. IR (solid, ATR) $\tilde{\nu}$ [cm^{-1}] = 3582 (w), 3287 (w), 2933 (br), 1647 (s), 1529 (w), 1497 (w), 1435 (m), 1383 (m), 1308 (m), 1207 (w), 1077 (s), 1013 (m), 937 (m), 890 (w), 811 (w), 773 (s), 702 (m), 670 (m), 656 (m), 621 (s), 537 (w), 520 (w), 403 (w).

Synthesis of Dy$_2$·Cl

The complex was isolated from an *in situ* reaction (Scheme 2). A mixture of $DyCl_3·6H_2O$ (1 mmol) and 3,5-diacetyl-4-methyl-1*H*-pyrazole (1 mmol) in 50 mL methanol was stirred and heated at 70 °C, then a solution of diethylenetriamine (1 mmol) in 20 mL methanol was added dropwise. The reaction was heated overnight at 70 °C. After the solution was allowed to cool to room temperature, the solvent was removed under vacuum and the residue was washed with ether to remove unreacted substrates. Pure colorless crystals of the product **Dy$_2$·Cl** were obtained by recrystallization of the crude product from methanol. Yield: 70 mg, (15%, based on metal salt). Elemental analysis (%) calcd for $[Dy_2L^2Cl_4]$ ($C_{24}H_{36}Cl_4Dy2N_{10}$, MW = 931.43): C, 30.95, H, 3.90, N, 15.04; found C, 29.88, H, 4.08, N, 14.31. IR (solid, ATR) $\tilde{\nu}$ [cm^{-1}] = 2922 (w), 2875 (w), 1610 (vs), 1504 (w), 1466 (w), 1455 (w), 1447 (w), 1418 (m), 1348 (m), 1292 (s), 1266 (w), 1208 (s), 1124 (m), 1096 (m), 1078 (m), 1050 (m), 1034 (s), 1012 (m), 967 (m), 933 (m), 827 (s), 749 (w), 721 (m), 553 (w), 532 (w), 479 (m), 426 (w).

Synthesis of Dy$_2^*$·Cl

The complex was isolated from an *in situ* reaction (Scheme 2). A mixture of $DyCl_3·6H_2O$ (1 mmol), and 3,5-diacetyl-4-methyl-1*H*-pyrazole (1 mmol) in 50 mL methanol was stirred and heated at 70 °C, then a solution of *N*,*N*-bis(2-aminoethyl) methylamine (1 mmol) in 20 mL methanol was added dropwise. The reaction was heated overnight at 70 °C. After the solution was allowed to cool to room temperature, the solvent was removed under vacuum and the residue was washed with ether to remove unreacted substrates. Pure colorless crystals of the product **Dy$_2^*$·Cl** were obtained by recrystallization of the crude product from methanol. Yield: 58 mg, (12%, based on metal salt). Elemental analysis (%) calcd for $[Dy_2L^3Cl_4]$ ($C_{26}H_{40}Cl_4Dy2N_{10}$, MW = 959.48): C, 32.55, H, 4.20, N, 14.60; found C, 31.39, H, 4.13, N, 13.95. IR (solid, ATR) $\tilde{\nu}$ [cm^{-1}] = 2906 (w), 1607 (vs), 1463 (w), 1433 (w), 1384 (w), 1348 (m), 1307 (w), 1294 (s), 1259 (w), 1211 (s), 1125 (m), 1094 (m), 1072 (w), 1049 (w), 966 (w), 927 (w), 779 (m), 724 (w), 554 (w), 539 (w), 479 (w), 427 (w).

Synthesis of Dy$_2$·NCS

Complex **Dy$_2$·NCS** was obtained from **Dy$_2$·Cl** by ligand substitution (Scheme 2). A mixture of **Dy$_2$·Cl** (0.1 mmol) and NH_4NCS (0.4 mmol) in 30 mL methanol was heated to 70 °C overnight without stirring, then the solution was slowly cooled to room temperature. Yellow crystals of complex **Dy$_2$·NCS** suitable for X-ray diffraction were obtained. Yield: 70 mg, (65%, based on **Dy$_2$·Cl**). Elemental analysis (%) calcd for $[Dy_2L^2(NCS)_4(MeOH)_2]$ ($C_{30}H_{44}Dy2N_{14}O_2S_4$, MW = 1086.03): C, 33.18, H, 4.08, N, 18.06, S, 11.81; found C, 31.80, H, 3.94, N, 18.16, S, 11.94. IR (solid, ATR) $\tilde{\nu}$ [cm^{-1}] = 2867 (w), 2931 (w), 2048 (vs), 1608 (s), 1465 (w), 1425 (s), 1352 (m), 1301 (s), 1210 (m), 1127 (m), 1100 (m), 1075 (s), 994 (w), 968 (s), 935 (s), 908 (m), 831 (m), 810 (m), 741 (w), 719 (m), 711 (m), 530 (w), 478 (m), 427 (w).

Crystallography

Crystal data and details of the data collections are given in Table S1.† X-ray data were collected on a STOE IPDS II diffractometer (graphite monochromated Mo-Kα radiation, λ = 0.71073 Å) by use of ω scans at −140 °C. The structures were solved with SHELXT and refined on F^2 using all reflections with SHELXL-2018.[36] Non-hydrogen atoms were refined anisotropically. Most hydrogen atoms were placed in calculated positions and assigned to an isotropic displacement parameter of 1.2/1.5 U_{eq}(C) and 1.2 U_{eq}(N) in case of **Dy$_2$·Cl**. The oxygen or nitrogen bound hydrogen atoms in **Dy$_4$** and **Dy$_2$·SCN** were refined using DFIX restraints ($d_{O\text{–}H}$ = 0.82 Å, $d_{N\text{–}H}$ = 1 Å (only for **Dy$_4$**)) and applying a fixed isotropic displacement parameter of 0.08 Å^2 in case of **Dy$_4$**. The counterions in **Dy4** (ClO_4^-) were found to disordered (occupancy factors: 0.879(5)/0.121(5) and 0.318(3)/0.682(3)). SADI ($d_{Cl\text{–}O}$ & $d_{O\cdots O}$) restraints and EADP constraints were applied to model the disordered parts.

The CH_3-$N(C_2H_4)_2$-moiety of the ligand in $\mathbf{Dy_2^*{\cdot}Cl}$ was found to be disordered (occupancy factors: 0.698(8)/0.302(8)). SADI ($d_{N–C}$ & $d_{C–C}$) and RIGU restraints were applied to model the disordered part. The unit cell of $\mathbf{Dy_4}$ contains highly disordered solvent molecules (DMF and H_2O) for which no satisfactory model for a disorder could be found. The solvent contribution to the structure factors was calculated with PLATON SQUEEZE[37] and the resulting .fab file was processed with SHELXL using the ABIN instruction. The empirical formula and derived values are in accordance with the calculated cell content. Face-indexed absorption corrections were performed numerically with the program X-RED. CCDC 2103370–2103373† contains the supplementary crystallographic data for this paper.

Magnetic measurements

Magnetic susceptibility measurements were recorded on a Quantum-Design MPMS XL-5 SQUID magnetometer equipped with a 5 T magnet. The fresh sample was transferred into a capsule and covered with perfluoropolyether based inert oil Fomblin Y45 to prevent any loss of solvent molecules. Direct current (dc) magnetic susceptibility measurements were performed on polycrystalline samples of $\mathbf{Dy_4}$, $\mathbf{Dy_2{\cdot}Cl}$, $\mathbf{Dy_2^*{\cdot}Cl}$, and $\mathbf{Dy_2{\cdot}SCN}$ in the temperature range 2–210 K (below the pour point of the oil Fomblin Y45), under an applied field of 5000 Oe (1000 and 5000 Oe for $\mathbf{Dy_4}$). The field-dependent magnetizations for all complexes were measured in the field range 0–5 T at 2 K. The dynamics of the magnetization were investigated by measuring the ac susceptibility under zero static field and a 3.0 Oe ac oscillating field. Diamagnetic corrections were made with the Pascal's constants[38] for all the constituent atoms as well as the experimentally determined contributions of the sample holder.

Conflicts of interest

The authors declare no competing financial interest.

Acknowledgements

J. W. thanks the Alexander von Humboldt Foundation for a postdoctoral fellowship.

Notes and references

1 (*a*) N. Ishikawa, M. Sugita, T. Ishikawa, S.-y. Koshihara and Y. Kaizu, *J. Am. Chem. Soc.*, 2003, **125**, 8694–8695; (*b*) P. Zhang and J. Tang, *Lanthanide Single Molecule Magnets*, Springer-Verlag, 2015; (*c*) A. Dey, P. Kalita and V. Chandrasekhar, *ACS Omega*, 2018, **3**, 9462–9475.

2 Z. Zhu, M. Guo, X.-L. Li and J. Tang, *Coord. Chem. Rev.*, 2019, **378**, 350–364.

3 (*a*) J. D. Rinehart and J. R. Long, *Chem. Sci.*, 2011, **2**, 2078–2085; (*b*) J.-L. Liu, Y.-C. Chen and M.-L. Tong, *Chem. Soc. Rev.*, 2018, **47**, 2431–2453.

4 (*a*) J. Wu, J. Jung, P. Zhang, H. Zhang, J. Tang and B. Le Guennic, *Chem. Sci.*, 2016, **7**, 3632–3639; (*b*) P. Cen, M. Wang, X. Ma, L. Chen, Y.-Q. Zhang, Y. Li, D. Tian and X. Liu, *CrystEngComm*, 2020, **22**, 6856–6863.

5 (*a*) Y.-C. Chen, J.-L. Liu, L. Ungur, J. Liu, Q.-W. Li, L.-F. Wang, Z.-P. Ni, L. F. Chibotaru, X.-M. Chen and M.-L. Tong, *J. Am. Chem. Soc.*, 2016, **138**, 2829–2837; (*b*) K.-X. Yu, J. G. C. Kragskow, Y.-S. Ding, Y.-Q. Zhai, D. Reta, N. F. Chilton and Y.-Z. Zheng, *Chem*, 2020, **6**, 1777–1793.

6 (*a*) A. Canaj, S. Dey, E. Regincós Marti, C. Wilson, G. Rajaraman and M. Murrie, *Angew. Chem., Int. Ed.*, 2019, **58**, 14146–14151; (*b*) Z.-H. Li, Y.-Q. Zhai, W.-P. Chen, Y.-S. Ding and Y.-Z. Zheng, *Chem. – Eur. J.*, 2019, **25**, 16219–16224.

7 (*a*) C. A. P. Goodwin, F. Ortu, D. Reta, N. F. Chilton and D. P. Mills, *Nature*, 2017, **548**, 439; (*b*) F. S. Guo, B. M. Day, Y. C. Chen, M. L. Tong, A. Mansikkamaki and R. A. Layfield, *Angew. Chem., Int. Ed.*, 2017, **56**, 11445–11449.

8 F.-S. Guo, B. M. Day, Y.-C. Chen, M.-L. Tong, A. Mansikkamäki and R. A. Layfield, *Science*, 2018, **362**, 1400–1403.

9 (*a*) H. L. C. Feltham and S. Brooker, *Coord. Chem. Rev.*, 2014, **276**, 1–33; (*b*) J. Hamacek and A. Vuillamy, *Eur. J. Inorg. Chem.*, 2018, 1155–1166.

10 (*a*) J. Acharya, N. Ahmed, J. Flores-Gonzalez, P. Kumar, F. Pointillart, O. Cador, S. K. Singh and V. Chandrasekhar, *Dalton Trans.*, 2020, **49**, 13110–13122; (*b*) H. Ke, Y. Yang, W. Wei, Y. Jiang, Y.-Q. Zhang, G. Xie and S. Chen, *Dalton Trans.*, 2020, **49**, 10594–10602.

11 (*a*) C. Jin, X.-L. Li, Z. Liu, A. Mansikkamäki and J. Tang, *Dalton Trans.*, 2020, **49**, 10477–10485; (*b*) Y. Huang, J.-X. Li, Y. Ge, X.-M. Zhang, Y. Xu, Y. Li, Y.-Q. Zhang and J.-L. Yao, *Dalton Trans.*, 2020, **49**, 8976–8984; (*c*) P. Cen, X. Liu, Y.-Q. Zhang, J. Ferrando-Soria, G. Xie, S. Chen and E. Pardo, *Dalton Trans.*, 2020, **49**, 808–816.

12 (*a*) D. Li, M.-M. Ding, Y. Ge, D. F. Tello Yepes, M. Sun, M. S. Najib, Y. Li, Y.-Q. Zhang and J.-l. Yao, *New J. Chem.*, 2020, **44**, 20634–20642; (*b*) F.-X. Shen, K. Pramanik, P. Brandão, Y.-Q. Zhang, N. C. Jana, X.-Y. Wang and A. Panja, *Dalton Trans.*, 2020, **49**, 14169–14179; (*c*) M. Kong, X. Feng, J. Wang, Y.-Q. Zhang and Y. Song, *Dalton Trans.*, 2020, **50**, 568–577.

13 (*a*) M. Fondo, J. Corredoira-Vázquez, A. M. Garcia-Deibe, J. Sanmartin Matalobos, S. Gómez-Coca, E. Ruiz and E. Colacio, *Inorg. Chem. Front.*, 2021, **8**, 2532–2541; (*b*) Y. Ge, D. Li, G. Wang, Y. Cui, M. S. Najib, Y. Li and B.-L. Wang, *Chem. – Asian J.*, 2019, **14**, 2846–2852.

14 (*a*) J. Wu, D. Liu, Q. Yang, Y. Ge, J. Tang and Z. Qi, *New J. Chem.*, 2021, **45**, 2200–2207; (*b*) S. Liu, J. Lu, X.-L. Li, Z. Zhu and J. Tang, *Dalton Trans.*, 2020, **49**, 12372–12379.

15 (*a*) H. Wada, S. Ooka, T. Yamamura and T. Kajiwara, *Inorg. Chem.*, 2017, **56**, 147–155; (*b*) Y.-S. Ding, T. Han, Y.-Q. Hu,

M. Xu, S. Yang and Y.-Z. Zheng, *Inorg. Chem. Front.*, 2016, **3**, 798–807.

16 (*a*) J. Wang, Z.-Y. Ruan, Q.-W. Li, Y.-C. Chen, G.-Z. Huang, J.-L. Liu, D. Reta, N. F. Chilton, Z.-X. Wang and M.-L. Tong, *Dalton Trans.*, 2019, **48**, 1686–1692; (*b*) H. L. C. Feltham, R. Clérac, A. K. Powell and S. Brooker, *Inorg. Chem.*, 2011, **50**, 4232–4234; (*c*) S.-G. Wu, Z.-Y. Ruan, G.-Z. Huang, J.-Y. Zheng, V. Vieru, G. Taran, J. Wang, Y.-C. Chen, J.-L. Liu, L. T. A. Ho, L. F. Chibotaru, W. Wernsdorfer, X.-M. Chen and M.-L. Tong, *Chem*, 2021, **7**, 982–992; (*d*) W. Rui-Chen, Wu Si-Guo, L. Jun-Liang, J. Jian-Hua, H. Guo-Zhang, Li Quan-Wen and T. Ming-Liang, *Acta Chim. Sin.*, 2020, **78**, 412–418.

17 J. Wang, Q.-W. Li, S.-G. Wu, Y.-C. Chen, R.-C. Wan, G.-Z. Huang, Y. Liu, J.-L. Liu, D. Reta, M. J. Giansiracusa, Z.-X. Wang, N. F. Chilton and M.-L. Tong, *Angew. Chem., Int. Ed.*, 2021, **60**, 5299–5306.

18 (*a*) B. Schneider, S. Demeshko, S. Dechert and F. Meyer, *Inorg. Chem.*, 2012, **51**, 4912–4914; (*b*) M. Steinert, B. Schneider, S. Dechert, S. Demeshko and F. Meyer, *Angew. Chem., Int. Ed.*, 2014, **53**, 6135–6139; (*c*) M. Steinert, B. Schneider, S. Dechert, S. Demeshko and F. Meyer, *Inorg. Chem.*, 2016, **55**, 2363–2373.

19 (*a*) G. Leibeling, S. Demeshko, S. Dechert and F. Meyer, *Angew. Chem., Int. Ed.*, 2005, **44**, 7111–7114; (*b*) D.-H. Manz, P.-C. Duan, S. Dechert, S. Demeshko, R. Oswald, M. John, R. A. Mata and F. Meyer, *J. Am. Chem. Soc.*, 2017, **139**, 16720–16731; (*c*) E. Ferretti, S. Dechert, S. Demeshko, M. C. Holthausen and F. Meyer, *Angew. Chem., Int. Ed.*, 2019, **58**, 1705–1709.

20 (*a*) S. J. Archibald, A. J. Blake, S. Parsons, M. Schröder and R. E. P. Winpenny, *J. Chem. Soc., Dalton Trans.*, 1997, 173–180; (*b*) S. J. Archibald, A. J. Blake, M. Schröder and R. E. P. Winpenny, *J. Chem. Soc., Chem. Commun.*, 1994, 1669–1670; (*c*) B. T. Gregg, K. C. Golden and J. F. Quinn, *Tetrahedron*, 2008, **64**, 3287–3295.

21 (*a*) Y.-N. Guo, L. Ungur, G. E. Granroth, A. K. Powell, C. Wu, S. E. Nagler, J. Tang, L. F. Chibotaru and D. Cui, *Sci. Rep.*, 2014, **4**, 5471; (*b*) J. Xiong, H.-Y. Ding, Y.-S. Meng, C. Gao, X.-J. Zhang, Z.-S. Meng, Y.-Q. Zhang, W. Shi, B.-W. Wang and S. Gao, *Chem. Sci.*, 2017, **8**, 1288–1294; (*c*) M. Guo, J. Wu, O. Cador, J. Lu, B. Yin, B. Le Guennic and J. Tang, *Inorg. Chem.*, 2018, **57**, 4534–4542; (*d*) M. Guo, Y.-Q. Zhang, Z. Zhu and J. Tang, *Inorg. Chem.*, 2018, **57**, 12213–12221.

22 (*a*) D. Casanova, P. Alemany, J. M. Bofill and S. Alvarez, *Chem. – Eur. J.*, 2003, **9**, 1281–1295; (*b*) S. Alvarez and M. Llunell, *J. Chem. Soc., Dalton Trans.*, 2000, 3288–3303.

23 (*a*) Y.-N. Guo, G.-F. Xu, W. Wernsdorfer, L. Ungur, Y. Guo, J. Tang, H.-J. Zhang, L. F. Chibotaru and A. K. Powell, *J. Am. Chem. Soc.*, 2011, **133**, 11948–11951; (*b*) S. K. Langley, C. Le, L. Ungur, B. Moubaraki, B. F. Abrahams, L. F. Chibotaru and K. S. Murray, *Inorg. Chem.*, 2015, **54**, 3631–3642; (*c*) S. K. Langley, L. Ungur, N. F. Chilton, B. Moubaraki, L. F. Chibotaru and K. S. Murray, *Inorg. Chem.*, 2014, **53**, 4303–4315.

24 (*a*) J. Tang, I. Hewitt, N. T. Madhu, G. Chastanet, W. Wernsdorfer, C. E. Anson, C. Benelli, R. Sessoli and A. K. Powell, *Angew. Chem., Int. Ed.*, 2006, **45**, 1729–1733; (*b*) L. Ungur, S.-Y. Lin, J. Tang and L. F. Chibotaru, *Chem. Soc. Rev.*, 2014, **43**, 6894–6905; (*c*) G. Fernandez Garcia, D. Guettas, V. Montigaud, P. Larini, R. Sessoli, F. Totti, O. Cador, G. Pilet and B. Le Guennic, *Angew. Chem., Int. Ed.*, 2018, **57**, 17089–17093.

25 N. F. Chilton, D. Collison, E. J. L. McInnes, R. E. P. Winpenny and A. Soncini, *Nat. Commun.*, 2013, **4**, 2551.

26 (*a*) L. F. Chibotaru, L. Ungur and A. Soncini, *Angew. Chem., Int. Ed.*, 2008, **47**, 4126–4129; (*b*) P.-H. Guo, J.-L. Liu, Z.-M. Zhang, L. Ungur, L. F. Chibotaru, J.-D. Leng, F.-S. Guo and M.-L. Tong, *Inorg. Chem.*, 2012, **51**, 1233–1235; (*c*) J. Wu, S.-Y. Lin, S. Shen, X.-L. Li, L. Zhao, L. Zhang and J. Tang, *Dalton Trans.*, 2017, **46**, 1577–1584.

27 (*a*) S.-Y. Lin, W. Wernsdorfer, L. Ungur, A. K. Powell, Y.-N. Guo, J. Tang, L. Zhao, L. F. Chibotaru and H.-J. Zhang, *Angew. Chem., Int. Ed.*, 2012, **51**, 12767–12771; (*b*) L. Ungur, S. K. Langley, T. N. Hooper, B. Moubaraki, E. K. Brechin, K. S. Murray and L. F. Chibotaru, *J. Am. Chem. Soc.*, 2012, **134**, 18554–18557; (*c*) K. R. Vignesh, S. K. Langley, A. Swain, B. Moubaraki, M. Damjanović, W. Wernsdorfer, G. Rajaraman and K. S. Murray, *Angew. Chem., Int. Ed.*, 2018, **57**, 779–784.

28 (*a*) I. F. Díaz-Ortega, J. M. Herrera, D. Aravena, E. Ruiz, T. Gupta, G. Rajaraman, H. Nojiri and E. Colacio, *Inorg. Chem.*, 2018, **57**, 6362–6375; (*b*) Y.-N. Guo, G.-F. Xu, P. Gamez, L. Zhao, S.-Y. Lin, R. Deng, J. Tang and H.-J. Zhang, *J. Am. Chem. Soc.*, 2010, **132**, 8538–8539; (*c*) L. Zhang, J. Jung, P. Zhang, M. Guo, L. Zhao, J. Tang and B. Le Guennic, *Chem. – Eur. J.*, 2016, **22**, 1392–1398.

29 D. Reta and N. F. Chilton, *Phys. Chem. Chem. Phys.*, 2019, **21**, 23567–23575.

30 (*a*) X.-L. Li, H. Li, D.-M. Chen, C. Wang, J. Wu, J. Tang, W. Shi and P. Cheng, *Dalton Trans.*, 2015, **44**, 20316–20320; (*b*) J. Wu, S. Demeshko, S. Dechert and F. Meyer, *Chem. Commun.*, 2020, **56**, 3887–3890.

31 (*a*) R. Orbach, *Proc. R. Soc. London, Ser. A*, 1961, **264**, 485–495; (*b*) R. Orbach, *Proc. R. Soc. London, Ser. A*, 1961, **264**, 458–484.

32 F.-S. Guo, A. Mansikkamaki, M.-L. Tong, Y.-C. Chen and R. Layfield, *Angew. Chem., Int. Ed.*, 2019, **58**, 10163–10167.

33 T. Han, Y. Ding, Z.-H. Li, K.-X. Yu, Y.-Q. Zhai, N. F. Chilton and Y.-Z. Zheng, *Chem. Commun.*, 2019, **55**, 7930–7933.

34 L. Ungur and L. F. Chibotaru, *Phys. Chem. Chem. Phys.*, 2011, **13**, 20086–20090.

35 A. Sachse, L. Penkova, G. Noël, S. Dechert, O. A. Varzatskii, I. O. Fritsky and F. Meyer, *Synthesis*, 2008, 800–806.

36 (*a*) G. M. Sheldrick, *Acta Crystallogr., Sect. C: Struct. Chem.*, 2015, **71**, 3–8; (*b*) G. M. Sheldrick, *Acta Crystallogr., Sect. A: Found. Adv.*, 2015, **71**, 3–8.

37 A. L. Spek, *Acta Crystallogr., Sect. C: Struct. Chem.*, 2015, **71**, 9–18.

38 E. A. Boudreaux and L. N. Mulay, *Theory and Applications of Molecular Paramagnetism*, John Wiley & Sons, New York, 1976.